DOI: 10.13009/EUCASS2023-464
Aerospace Europe Conference 2023 – 10TH EUCASS – 9TH CEAS

ReFEx: Reusability Flight Experiment - Design of an Exoatmospheric Control System

Johannes Robens[⋆†], *Björn Gäßler*[⋆] *and Paul Acquatella B.*[⋆]
[⋆]*German Aerospace Center (DLR), Institute of System Dynamics and Control*
Münchener Straße 20, 82234 Weßling, Germany
johannes.robens@dlr.de · bjoern.gaessler@dlr.de · paul.acquatella@dlr.de
[†]Corresponding author

Abstract

This paper presents the control system design for the exoatmospheric flight of the ReFEx mission. The trajectory is planned by means of spherical linear interpolation and polynomial progression. Due to discrete firing actuators, a PD-controller including a deadband is implemented and augmented by partial feedback linearization to allow controller gain design through pole placement. A pulse-width pulse-frequency modulation scheme, capable of considering switching restrictions, is employed to interface the continuous torque commands with the thrusters. Additionally, the control allocation strategy enables compensation for up to two thruster failures. Monte-Carlo simulations finally demonstrate the performance and robustness of the control system.

1. Introduction

Within the "Reusability Flight Experiment" (ReFEx) project, the German Aerospace Center (DLR) has set the objective of demonstrating the return flight of an aerodynamically controlled reusable launch vehicle (RLV) from hypersonic to transonic region. This endeavor allows DLR to acquire significant expertise in this domain and gather essential flight data pertaining to a winged RLV stage. The collected data serves to validate design tools utilized for this type of systems, thereby enabling DLR to actively contribute to future national and international advancements in the field of reusable launch vehicles.

The demonstrator is scheduled to launch on a Brazilian sounding rocket from Koonibba Test Range in South Australia in 2024. Following separation from the rocket at an altitude of approximately 85 km, the vehicle will traverse a ballistic flight path in the exoatmospheric region, reaching an apogee of approximately 130 km, before reentering earth's atmosphere at hypersonic speeds. During this phase, the vehicle's attitude will be controlled by a reaction control system (RCS). Starting from an altitude of around 50 km, aerodynamic forces will significantly influence the vehicle due to a rising dynamic pressure. As a result, an aerodynamic control system is employed in place of the exoatmospheric control system marking the transition to aerodynamic controls. To demonstrate controllability and maneuverability, the vehicle will perform a heading change of more than 30° . The experiment will conclude at an altitude of approximately 7 km, with the vehicle maintaining subsonic velocity and the aim to reach a target ellipsoid. Throughout the entire flight, the vehicle will be guided and controlled until its belly landing. For a more comprehensive overview of the mission, refer to [7].

This paper provides a detailed explanation of the design of the control system employed during the exoatmospheric flight to regulate the vehicle's attitude. The following section (2) focuses on the influence of the vehicle's structure on the control system design, as well as various maneuvers performed during the exoatmospheric phase. Subsequently, in section 3, the trajectory planning for the several maneuvers is explained in detail. The fourth section introduces the controller design along with the corresponding gains determined through pole placement according to desired closed-loop error dynamics. The control allocation methodology is then described in section 5, which utilizes pulse-width pulse-frequency (PWPF) modulation to allocate continuous commanded torques to discrete firing thrusters. Finally, the performance and robustness are evaluated by the nominal case as well as Monte-Carlo simulations in section 6.

DOI: 10.13009/EUCASS2023-464

2. Vehicle and Mission Description

This section provides a brief introduction to the general structure of the vehicle, including a closer look at the reaction control system and its mass properties that influence the selection of the control system. Subsequently, the maneuvers are described that need to be performed during the exoatmospheric phase before reentering earth's atmosphere. The criteria to terminate and proceed with the subsequent maneuver are also defined.

2.1 Vehicle Description

The general structure of the vehicle is shown in Figure 1, featuring a length of 2.7 m, a wingspan of 1.1 m, and an approximate mass of 400 kg. Positioned at the front of the vehicle are individually deflectable canards, while a rudder is located at the vertical tail to complement the aerodynamic set of actuators for full 3-axis attitude control. To facilitate the exoatmospheric phase of the flight, a reaction control system is incorporated at the rear of the vehicle. Figure 1 also illustrates the body frame of the system since the angular motion (angular rates and accelerations) is considered in this frame. The origin is situated at the nominal center of mass, which is located 57 % of the vehicle's total length behind the nose by design. The body's x- and z-axes align with the symmetry plane with the x-axis pointing towards the nose and the z-axis oriented towards the bottom. The y-axis completes the right-handed body frame.

The configuration of the reaction control system is outlined in Figure 2. It comprises eight cold gas thrusters that utilize pressurized nitrogen as their propellant. Each thruster is primarily dedicated to generating a torque around one of the body axes. Thrusters 7 and 8 accelerate the vehicle around its y-axis by applying a pitch torque. Similarly, thrusters 5 and 6 produce a yaw torque around the z-axis. As a difference, thrusters 1 and 4, as well as 2 and 3, must fire simultaneously to apply a roll torque exclusively around the vehicle's x-axis. While they can also contribute to pitch torque, they provide redundancy around the y-axis, such that only a yaw thruster failure cannot be compensated. This will be further discussed in section 5. Furthermore, several other aspects of the RCS influence the design of the control system. Firstly, all thrusters can be operated in either a low or high thrust mode, providing approximately 2.16 N or 8.92 N of thrust, respectively. As the switching time between these modes is significant, it is crucial to establish clear guidelines for their usage. Due to limitations of the pressure reducers, the actual thrust also depends on the number of engines firing simultaneously. When two valves are open, each thrust is reduced to 91 % of its nominal value. Similarly, the derating factors for three- and four open valves are 73 % and 65 %, respectively. Another important aspect is the time behavior of the thrust. Due to signal processing delays and the transient behavior of gas flow, there is a delayed response to control commands. Consequently, the full thrust is attained 22 ms after sending the open command, while it takes 45 ms to return to zero thrust when the valve is closed. Further information on the setup of the reaction control system and experimental tests can be found in Hoffmeister et al [3].

To facilitate trajectory planning and the determination of control gains, it is essential to have estimates of the maximum angular accelerations that the thrusters can generate. Therefore, certain parameters need to be known including the nominal thrust F_{nom}, the number of active thrusters n_t, their lever arm l, and the moment of inertia $\boldsymbol{J}$. With this information, the maximum acceleration can be calculated using Equation 1, formulated for the x-direction while the same applies for the remaining axes. Here, l_x represents the lever arm of the thrusters and $n_{t,x}$ the number of thrusters that generate a roll torque in the same direction to the body frame's x-axis. The moment of inertia is reduced to its diagonal element of the x-axis J_{xx}.

$$\dot{\omega}_{max,x} = \frac{l_x \, n_{t,x} \, F_{nom}}{J_{xx}} \tag{1}$$

As described in section 5, the vehicle is rotated around its z-axis by only one thruster. In contrast, a roll torque is generated by two thrusters, while a pure pitch moment utilizes three simultaneous thrusters. However, due to a derating factor of 73 % for three open valves, only two firing thrusters are considered for calculating the maximum pitch acceleration. These considerations result in the estimated maximum angular accelerations for the low and high thrust modes, as provided in Equation 2 and Equation 3.

$$\text{Low thrust mode:} \quad \dot{\boldsymbol{\omega}}^{l}_{max} = (0.037\,, 0.019\,, 0.009)^T \ \text{rad}\,\text{s}^{-2} \tag{2}$$

$$\text{High thrust mode:} \quad \dot{\boldsymbol{\omega}}^{h}_{max} = (0.152\,, 0.077\,, 0.038)^T \ \text{rad}\,\text{s}^{-2} \tag{3}$$

DOI: 10.13009/EUCASS2023-464

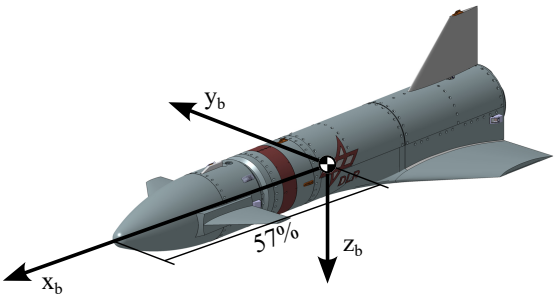

Figure 1: Vehicle structure and body frame representation.

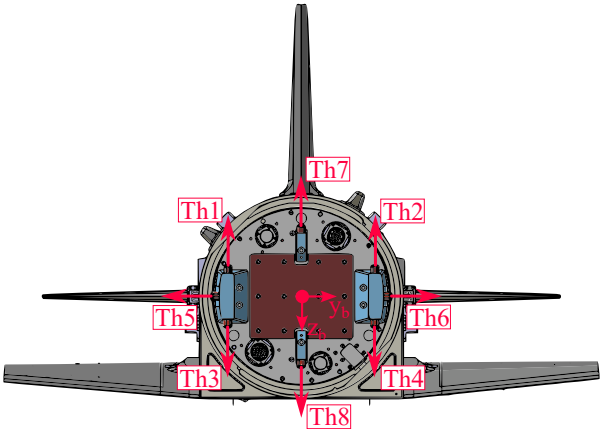

Figure 2: Thruster layout [3].

2.2 Mission Description: Focus on Exoatmospheric Phase

The exoatmospheric phase of the flight is depicted in Figure 3, which illustrates the vehicle's geodetic altitude over time including the various modes of this phase. The actual flight of the demonstrator starts with its separation from the carrier rocket, occurring approximately 94 s after lift-off. Throughout the launch, the actuators remain locked to prevent unintended influence on the rocket's dynamics. However, within the first 5 s after separation, they are unlocked to enable control of the vehicle. This phase is referred to as the "no control mode" (NCM). After separation, due to the residual spin from the passively controlled rocket and the perturbation rates arising from the separation process, the vehicle undergoes tumbling. Consequently, the initial controlled maneuver aims to reduce the vehicle's angular rate below a predefined threshold during the "rate damping mode" (RDM1). Following the detumbling, the vehicle's longitudinal axis needs to be aligned with an axis perpendicular to the sun direction. The final state of the reorientation is determined when both the total attitude error, expressed as the quaterion Euler angle error, and the angular rate error fall below predefined thresholds. The mode employed during this phase is referred to as the "sun acquisition mode" (SAM). Following the SAM, the vehicle rotates around the body's x-axis known as the "sun scanning mode" (SSM) to calibrate the navigation system. During this mode, multiple sun sensors oriented in various directions detect the sun, significantly enhancing state estimation and navigation solution. Given its critical importance in the exoatmospheric phase of the flight, the SSM is sustained for as long as possible. Ultimately, it is terminated at a predefined altitude to allow sufficient time for vehicle reorientation in preparation for atmospheric reentry. Afterwards, a second execution of the "rate damping mode" (RDM2) is carried out for 8 s to eliminate any residual vehicle rotation. Subsequently, during the "entry attitude acquisition mode" (EAM), the vehicle reorients itself again towards the final desired state for atmospheric reentry in terms of the aerodynamic angles angle of attack, angle of sideslip and bank angle. The EAM is concluded at a predefined altitude, at which point the guidance system begins providing continuous guidance signals in terms of aerodynamic angles. Finally, the "guided entry exoatmospheric mode" (GEEM) follows the guided attitude until the dynamic pressure reaches a level sufficient for the aerodynamic control system to assume control. In general, the low thrust mode is employed to achieve attitude control with higher precision. However, towards the end of the exoatmospheric flight, specifically during the "entry attitude acquisition mode" (EAM) and "guided entry exoatmospheric mode" (GEEM), the dynamic pressure begins to rise. This increase leads to aerodynamic disturbance forces and moments, among other factors, caused by inaccurately trimmed aerodynamic control surfaces. To counteract these disturbances and maintain effective thruster performance for as long as possible, the high thrust mode is utilized instead.

3. Trajectory Planning

For each of the modes in the exoatmospheric phase, except GEEM, the guidance system provides a desired state, but does not specify how the vehicle should transition to that state. The separation between trajectory planning and error control allows for additional degrees of freedom in the design. By designing the control system to focus solely on controlling errors from a reference trajectory, overall performance can be enhanced. While the control system is described in the next section, this section focuses on the trajectory planning.

DOI: 10.13009/EUCASS2023-464

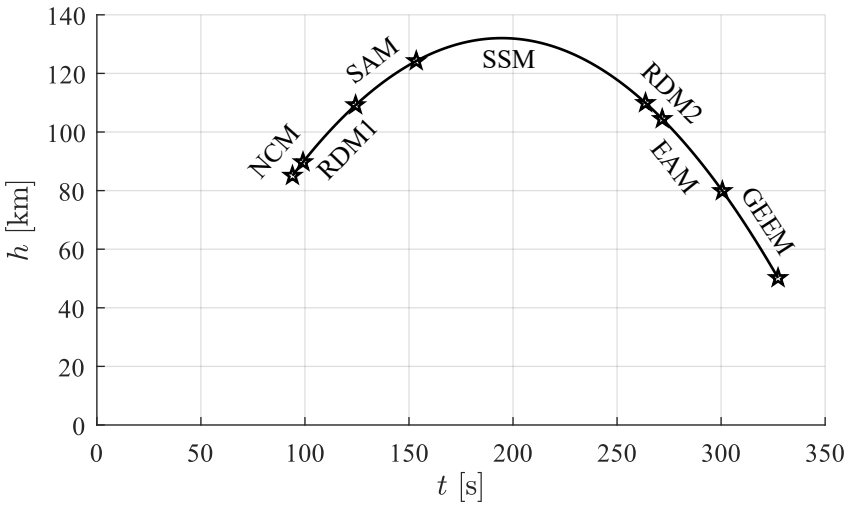

Figure 3: Exoatmospheric modes of the flight.

3.1 Sun Acquisition Mode (SAM) and Entry Attitude Acquisition Mode (EAM)

During SAM and EAM, a reorientation of the vehicle is commanded with stationary initial and final states, meaning that it does not change its inertial attitude and is not angularly accelerated. As the vehicle's attitude is represented using quaternions with the fourth component being the scalar part, the spherical linear interpolation (SLERP) technique [2] is employed. SLERP, which is given in Equation 4, enables the vehicle to follow the shortest arc on the quaternion unit sphere by taking equal angular steps. Here, $h \in [0, 1]$ represents the interpolation variable, while q_0, q_1, and q_h denote the initial, the final and the interpolated quaternion at h, respectively.

$$\begin{gathered} \cos(\Omega) = \boldsymbol{q}_0 \cdot \boldsymbol{q}_1 \\ \boldsymbol{q}_h = \frac{\boldsymbol{q}_0 \sin((1-h)\,\Omega) + \boldsymbol{q}_1 \sin(h\,\Omega)}{\sin(\Omega)} \end{gathered} \tag{4}$$

As a quaternion and its negative represent the same attitude, two different vectors can be utilized to express the final orientation. Typically, these vectors have different arc lengths on the quaternion unit sphere, originating from the initial attitude. Consequently, it is crucial to select the quaternion with the shorter arc length as the final attitude to ensure that SLERP interpolates along the shortest rotation path. The transition is fully determined by defining the interpolation variable $h = h(t)$ starting at $t_0 = 0$. In general, the maneuvers are subject to constraints on attitude, rate, and acceleration for both the initial and final states. A polynomial with a degree one less than the number of constraints can be precisely defined by the imposed restrictions, resulting in a desired transition without non-essential motion. Since SAM and EAM describe similar maneuvers, they have identical constraints. The initial state is required to be stationary and identical to the initial attitude. At the end of the transition ($t = t_1$), the vehicle should reach the final attitude stationary. These constraints are mathematically formulated next.

$$h(t=0) = 0 \qquad \dot{h}(t=0) = 0 \qquad \ddot{h}(t=0) = 0 \tag{5}$$

$$h(t=t_1) = 1 \qquad \dot{h}(t=t_1) = 0 \qquad \ddot{h}(t=t_1) = 0 \tag{6}$$

As a result, the following 5^{th} degree polynomial and its first two derivatives can be derived.

$$h(t) = \frac{6}{t_1^5}t^5 - \frac{15}{t_1^4}t^4 + \frac{10}{t_1^3}t^3 \tag{7}$$

$$\dot{h}(t) = \frac{30}{t_1^5}t^4 - \frac{60}{t_1^4}t^3 + \frac{30}{t_1^3}t^2 \tag{8}$$

$$\ddot{h}(t) = \frac{120}{t_1^5}t^3 - \frac{180}{t_1^4}t^2 + \frac{60}{t_1^3}t \tag{9}$$

DOI: 10.13009/EUCASS2023-464

The rotation defined by SLERP can also be expressed by a fixed Euler axis $\boldsymbol{e}$ and Euler angle θ. Therefore, it can be represented by a rotation around a single axis resulting in direct integral relations between angular acceleration, rate and angle. Here, the rotation around each axis of the body frame is defined by the vector $\boldsymbol{\theta} = \boldsymbol{e}\,\theta$. At time t, the commanded rotation angles in body frame $\boldsymbol{\phi}(t)$ can be calculated by multiplying the total rotation angle vector $\boldsymbol{\theta}$ and the interpolation variable $h(t)$. By deriving this equation twice, the corresponding angular rate $\boldsymbol{\omega}$ and acceleration $\dot{\boldsymbol{\omega}}$ are obtained. Since $\boldsymbol{\theta}$ is constant, only the interpolation variable $h(t)$ has to be derived. This results in the following equations.

$$\boldsymbol{\phi}(t) = \boldsymbol{\theta}\, h(t) \tag{10}$$

$$\boldsymbol{\omega}(t) = \boldsymbol{\theta}\, \dot{h}(t) \tag{11}$$

$$\dot{\boldsymbol{\omega}}(t) = \boldsymbol{\theta}\, \ddot{h}(t) \tag{12}$$

To fully define the interpolation variable h and, consequently, its transition, the end time t_1 needs to be determined. In order to allow margin for error control, it is generally recommended to reserve some of the thrusters' capabilities rather than utilizing their full potential. As a result, the angular accelerations are limited to 65 % of the maximum angular accelerations achievable by the thrusters, as indicated in Equation 2 and Equation 3. The superscript l/h denotes the possible use of either the low or high thrust mode values. This value corresponds to the derating factor when four valves are open, which already significantly reduces maneuverability. However, it still provides a margin in case fewer thrusters are firing simultaneously, which is typically the case. The minimum end time $t_{1,min}$ can be calculated using Equation 13, which considers the longest duration among the body axes.

$$\begin{aligned} \dot{\boldsymbol{\omega}}_{max} &= 0.65\, \dot{\boldsymbol{\omega}}_{max}^{l/h} \\ t_{1,min} &= \max\left(\left(\frac{20\,|\boldsymbol{\theta}|}{12^{1/2}\,\dot{\boldsymbol{\omega}}_{max}}\right)^{1/2}\right) \end{aligned} \tag{13}$$

In addition, a design time $t_{1,dsgn}$ can be manually defined, if a fixed duration can be assigned to a maneuver under all uncertainties and perturbations. The higher value is chosen as the actual duration for the maneuver to be more fuel efficient.

$$t_1 = \max\left(t_{1,min}\,, t_{1,dsgn}\right) \tag{14}$$

Finally, when the time $t > t_1$, the final state is set as the desired state for the remainder of the mode. To conclude, Equation 4 is employed to calculate the desired attitude signal represented as a quaternion, while Equation 11 and Equation 12 define the corresponding angular rate and acceleration reference signals, respectively. Figure 4 presents representative curves illustrating the trajectory planning for the sun acquisition mode.

3.2 Rate Damping Mode (RDM)

Since the rate damping mode only commands angular rates to zero, a quaternion interpolation is not necessary and a polynomial expression is sufficient to define the maneuver. Thus, the attitude of the vehicle is not controlled during this phase of the flight. In contrast to SAM and EAM, the polynomial directly describes the desired trend of the angular rates. As such, the initial state is required to have no angular acceleration and to be identical to the initial rates of the vehicle $\boldsymbol{\omega}_0$. At the end of the transition, the vehicle should be stationary.

$$\boldsymbol{\omega}(t=0) = \boldsymbol{\omega}_0 \qquad \dot{\boldsymbol{\omega}}(t=0) = \mathbf{0} \tag{15}$$

$$\boldsymbol{\omega}(t=t_1) = \mathbf{0} \qquad \dot{\boldsymbol{\omega}}(t=t_1) = \mathbf{0} \tag{16}$$

Due to the number of constraints, a 3$^{\text{rd}}$ degree polynomial and its first derivative can be derived.

$$\boldsymbol{\omega}(t) = \left(\frac{2}{t_1^3}t^3 - \frac{3}{t_1^2}t^2 + 1\right)\boldsymbol{\omega}_0 \tag{17}$$

$$\dot{\boldsymbol{\omega}}(t) = \left(\frac{6}{t_1^3}t^2 - \frac{6}{t_1^2}t\right)\boldsymbol{\omega}_0 \tag{18}$$

DOI: 10.13009/EUCASS2023-464

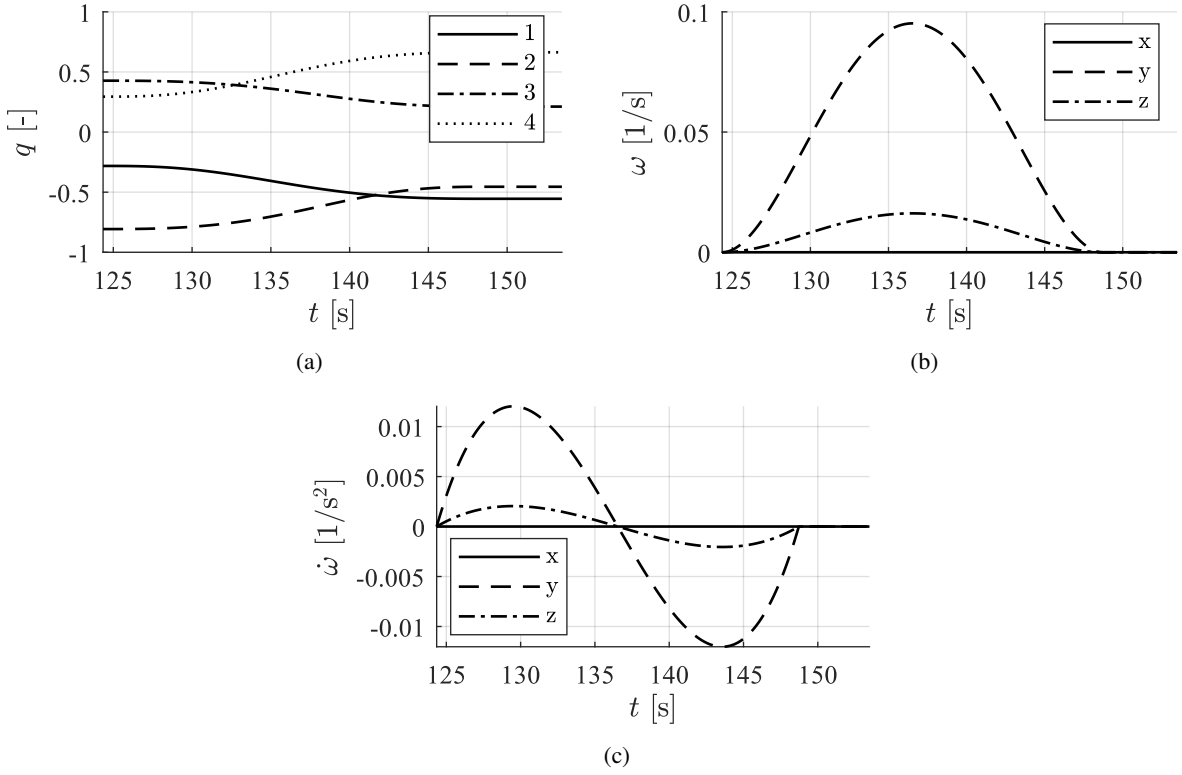

Figure 4: Representative curves for trajectory planning of SAM. (a) Attitude expressed as a quaternion, (b) angular rate and (c) angular acceleration.

Lastly, the end time t_1 needs to be determined. In this case, a similar approach as for SAM and EAM is employed, without a predefined end time $t_{1,dsgn}$ since slower maneuvers still consume the same amount of fuel. However, to mitigate induced oscillations and ensure a smoother transition, a 3$^{\text{rd}}$ degree polynomial is chosen. Consequently, the end time is calculated using Equation 19. For times $t > t_1$, the final state is considered to be the desired state.

$$t_1 = \max\left\{\frac{3}{2}\frac{|\omega_{0,x}|}{\dot{\omega}_{max,x}}, \frac{3}{2}\frac{|\omega_{0,y}|}{\dot{\omega}_{max,y}}, \frac{3}{2}\frac{|\omega_{0,z}|}{\dot{\omega}_{max,z}}\right\} \tag{19}$$

3.3 Sun Scanning Mode (SSM)

The trajectory planning for the sun scanning mode can also directly apply the polynomial to rotational states. In contrast to the rate damping mode, the vehicle begins stationary and concludes with a constant angular rate. To stabilize the rotation axis, the attitude is also controlled throughout this phase, necessitating the determination of a desired quaternion signal. There exists a direct integral relationship between angular acceleration, rate, and angle, as they can be expressed as scalars with reference to a fixed axis around which the vehicle rotates. By multiplying these scalar values with the rotation axis, a vectorial expression in the body frame is obtained. Thus, the polynomial represents the angle, while its first two derivatives define angular rate and acceleration. The sun scanning mode encompasses five constraints. The entire initial state is confined to zero values and at the end of the transition, only the rate and acceleration are constrained to be identical to a predefined rate $\boldsymbol{\omega}_1$ and zero, respectively.

$$\boldsymbol{\phi}(t=0) = \mathbf{0} \qquad \boldsymbol{\omega}(t=0) = \mathbf{0} \qquad \dot{\boldsymbol{\omega}}(t=0) = \mathbf{0} \tag{20}$$

$$\boldsymbol{\omega}(t=t_1) = \boldsymbol{\omega}_1 \qquad \dot{\boldsymbol{\omega}}(t=t_1) = \mathbf{0} \tag{21}$$

This leads to a 4$^{\text{th}}$ degree polynomial. Since the final state is not stationary, the angle $\boldsymbol{\phi}$ increases linearly, when the time exceeds t_1. The time dependent desired states are shown hereafter.

DOI: 10.13009/EUCASS2023-464

$t \leq t_1$:

$$\boldsymbol{\phi}(t) = \left(-\frac{1}{2\,t_1^3}t^4 + \frac{1}{t_1^2}t^3\right)\boldsymbol{\omega}_1 \tag{22}$$

$$\boldsymbol{\omega}(t) = \left(-\frac{2}{t_1^3}t^3 + \frac{3}{t_1^2}t^2\right)\boldsymbol{\omega}_1 \tag{23}$$

$$\dot{\boldsymbol{\omega}}(t) = \left(-\frac{6}{t_1^3}t^2 + \frac{6}{t_1^2}t\right)\boldsymbol{\omega}_1 \tag{24}$$

$t > t_1$:

$$\boldsymbol{\phi}(t) = \boldsymbol{\phi}(t_1) + \boldsymbol{\omega}_1\ (t - t_1) \tag{25}$$

$$\boldsymbol{\omega}(t) = \boldsymbol{\omega}_1 \tag{26}$$

$$\dot{\boldsymbol{\omega}}(t) = \mathbf{0} \tag{27}$$

In order to obtain a desired attitude expressed as a quaternion, the angle vector $\boldsymbol{\phi}$ can be transformed to a quaternion and subsequently multiplied with the desired initial quaternion of the sun scanning mode. Finally, the end time t_1 is determined identical to rate damping mode by Equation 19 with $\boldsymbol{\omega}_0$ substituted by $\boldsymbol{\omega}_1$.

4. Controller Design

This chapter introduces the controller design that is used for all the modes of the exoatmospheric part of the flight. In this design, the choice of low or high thrust mode only influences the control gains. The full dynamics of the vehicle are described by the quaternion kinematics [5] and Euler's moment equations [8] that are shown in Equation 28 and Equation 29. Here, $\boldsymbol{u}$ represents the vectorial input of the system, while $\boldsymbol{\Xi}(\boldsymbol{q})$ is a quaternion matrix defined in Markley et al [5].

$$\dot{\boldsymbol{q}} = \frac{1}{2}\boldsymbol{\Xi}(\boldsymbol{q})\,\boldsymbol{\omega} \tag{28}$$

$$\dot{\boldsymbol{\omega}} = \boldsymbol{J}^{-1}\left(\boldsymbol{u} - \boldsymbol{\omega} \times \boldsymbol{J}\,\boldsymbol{\omega}\right) \tag{29}$$

To achieve a controlled system that behaves close to a double integrator system, the Euler's moment equations are compensated by feedback linearization [9]. By choosing the input $\boldsymbol{u}$ as shown in Equation 30, the controlled system is simply reduced to $\dot{\boldsymbol{\omega}} = \boldsymbol{\nu}$, when the quaternion kinematics are neglected, with $\boldsymbol{\nu}$ representing the controller output.

$$\boldsymbol{u} = \boldsymbol{J}\,\boldsymbol{\nu} + \boldsymbol{\omega} \times \boldsymbol{J}\,\boldsymbol{\omega} \tag{30}$$

The one dimensional error dynamics of a scalar double integrator system with a PD-controller and a feed-forward term in the loop can be described by Equation 31. Here, the error e is defined as the difference between the current state x and the desired state x_g. Furthermore, K_p and K_d denote the proportional and the derivative gain of the controller.

$$\begin{gathered} e = x - x_g \\ \ddot{e} + K_d\,\dot{e} + K_p\,e = 0 \end{gathered} \tag{31}$$

By comparing the coefficients with the homogeneous equation of a mass-spring-damper model (Equation 32), a relation between the control gains and the damping ζ and natural frequency ω_n of this model can be obtained. They are given in Equation 33 and Equation 34. As a result, the control gains can be chosen, such that the system is asymptotically stable and does not overshoot by setting the damping $\zeta \geq 1$.

$$\ddot{x} + 2\,\zeta\,\omega_n\,\dot{x} + \omega_n^2\,x = 0 \tag{32}$$

$$K_p = \omega_n^2 \tag{33}$$

$$K_d = 2\,\zeta\,\omega_n = 2\,\zeta\,K_p^{1/2} \tag{34}$$

DOI: 10.13009/EUCASS2023-464

In the ReFEx case, a PD-controller including a feed-forward term is chosen (Equation 35), but the proportional part is defined with respect to a quaternion error $\boldsymbol{q}_e$, while the derivative part and the feed-forward term relate to rate error $\boldsymbol{\omega}_e$ and guidance angular acceleration $\dot{\boldsymbol{\omega}}_g$, respectively. In addition, the gains are defined as diagonal matrices.

$$\boldsymbol{\nu} = \dot{\boldsymbol{\omega}}_g - \boldsymbol{K}_d\,\boldsymbol{\omega}_e - \boldsymbol{K}_p\,\boldsymbol{q}_e \tag{35}$$

Since rate and quaternion errors do not have a direct integral relation, the behavior does not exactly match the one of the double integrator system. This could be achieved by also compensating the quaternion kinematics, which would lead to a full feedback linearization as described by Bang et al [1]. As a compromise, only the attitude error expressed as a quaternion would be present in the proportional part of the controller, while the rate error and angular acceleration are substituted by other terms. This approach was tested, but does not control the rate error explicitly. Therefore, the controller of Equation 35 in combination with the partial feedback linearization by Equation 30 is used to calculate the commanded torques $\boldsymbol{\tau}_c = \boldsymbol{u}$ during the exoatmospheric part of the flight.

Although the designed controller does not exactly match the error dynamics of Equation 31, the relations for the controller gains in Equation 33 and Equation 34 are still used to find reasonable solutions analytically. Since cold gas thrusters are discrete firing actuators and only a limited amount of propellant is available, they are not activated before the commanded torque exceeds a threshold. As a result, there is a deadband in which state errors are not corrected. For special cases, the attitude error can be related to the minimum required torque by means of the proportional gain $\boldsymbol{K}_p$. Thus, the gain can be used to define the deadband size for attitude errors. Assuming the vehicle is stationary ($\boldsymbol{\omega} = \boldsymbol{0}$) and the guidance acceleration ($\dot{\boldsymbol{\omega}}_g$) as well as the rate error ($\boldsymbol{\omega}_e$) are equal to $\boldsymbol{0}$, the commanded torques reduces to Equation 36.

$$\boldsymbol{\tau}_c = \boldsymbol{u} = -\boldsymbol{J}\,\boldsymbol{K}_p\,\boldsymbol{q}_e \tag{36}$$

If, in addition, the attitude error is assumed to be around one axis and the moment of inertia matrix is reduced to the main element of that axis, which is reasonable due to the ratio of the largest off-diagonal and smallest diagonal element being already less than 8.5 %, an analytical expression for the proportional gain can be derived. The result is shown in Equation 37 for the body's x-axis. The same applies for the remaining axes. Here, ϕ_e represents the angle error.

$$K_{p,x} = \frac{-\tau_{c,x}}{J_{xx}\sin\left(\frac{1}{2}\,\phi_e\right)} \tag{37}$$

As explained in the next section, the thrusters are opened, if the commanded torque exceeds 35 % of the maximum producible torque. To calculate the proportional gains, the maximum accelerations $\dot{\boldsymbol{\omega}}^{l/h}_{max}$ of Equation 2 and Equation 3 can be integrated in Equation 37 as shown in Equation 38. Since the controller design requires the gains to always be positive, the absolute value is taken. Furthermore, the angle error is replaced by the limit angle of the deadband $\phi_{e,db}$, which is set to $\pm 0.42°$.

$$K_{p,x} = \left|\frac{0.35\,\dot{\omega}^{l/h}_{max,x}}{\sin\left(\frac{1}{2}\,\phi_{e,db}\right)}\right| \tag{38}$$

Subsequently, the derivative gains can be determined by Equation 34 with a damping $\zeta = 1$. Thereby, the fuel consumption is reduced, since the vehicle does not overshoot during rotations. The final sets of gains for low and high thrust are shown in Table 1a and Table 1b, sorted by the body axes.

Table 1: Set of Exoatmospheric Control Gains.

(a) Low Thrust

	$\boldsymbol{K_p}$	$\boldsymbol{K_d}$
X	3.55	3.77
Y	1.79	2.68
Z	0.88	1.88

(b) High Thrust

	$\boldsymbol{K_p}$	$\boldsymbol{K_d}$
X	14.69	7.67
Y	7.41	5.45
Z	3.65	3.82

DOI: 10.13009/EUCASS2023-464

5. Control Allocation Design

The controller in section 4 commands continuous torque signals. Ideally, these torques are perfectly applied to the vehicle by appropriate actuators. Since the vehicle is equipped with a reaction control system that consists of eight cold gas thrusters, only fixed torque values can be generated. Therefore, the goal of the control allocation design is to connect the continuous controller signals with the discrete firing actuator system and to allocate the commanded torques to suitable thrusters while having possible thruster failures in mind.

A common approach to realize the torque signal is by using either a pulse-width (PW), a pulse-frequency (PF), or a combined PWPF modulation. Since the controller only outputs torque values at discrete time points, the general idea of these methods is to produce an average torque within the controller sampling time, which matches the commanded torque, by adapting the thrusters' activation times. This requires the actuator system to run on a higher frequency than the controller. Kienitz et al [4] developed a software based PWPF modulation scheme that allows the controller and control allocation to run on the same comparably high frequency. As a result, the realization of the commanded torques is more accurate than conventional pulse modulation techniques ([10], [8]) with no transition problems between consecutive time intervals. Furthermore, the scheme inherently considers switching restrictions like minimum pulse duration t_{on} and minimum rest between successive pulses t_{off}.

A generic pulse modulator output $w(t) \in \{-1, 0, 1\}$ is shown in Figure 5. Due to $w(t)$ being defined for every body axis, the vehicle accelerates in positive direction around this axis when $w(t) = 1$, does not accelerate for $w(t) = 0$, and generates a negative torque for $w(t) = -1$. Nevertheless, each torque should be generated by a fixed separated set of thrusters, such that their activities are represented by one pulse modulator output. The duration of pulse k of $w(t)$ is denoted by γ_k, while the time interval between start of pulse k and start of pulse $k+1$ of $w(t)$ is referred to as T_k.

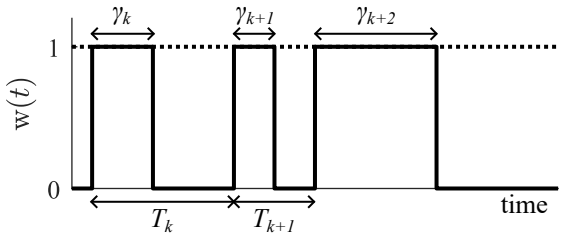

Figure 5: Generic pulse modulator output $w(t)$ [4].

Due to the switching restrictions, γ_k and T_k have to fulfill the inequalities in Equation 39 and Equation 40.

$$\gamma_k \geq t_{on} \tag{39}$$

$$T_k \geq \gamma_k + t_{off} \tag{40}$$

The pulse modulation scheme by Kienitz et al [4] transforms the controller output to on/off-commands for the actuators, as follows, and notice it is identically applied to each of the body axes. First, the commanded torque is modified by an arbitrary function $f(\tau_c)$. This function is set equal to the average torque that is generated by the pulse modulator $\overline{\tau}$ in Equation 41. Here, τ_{max} is the maximum producible torque. Since the sign of the modulator output $w(t)$ depends directly on the sign of $f(\tau_c)$, Equation 41 leads to Equation 42.

$$f(\tau_c) = \overline{\tau} = \frac{\text{sign}\left(f(\tau_c)\right)\tau_{max}\,\gamma_k}{T_k} \tag{41}$$

$$|f(\tau_c)| = \frac{\tau_{max}\,\gamma_k}{T_k} \tag{42}$$

Although $f(\tau_c)$ can be an arbitrary function, it is very reasonable to define the function such that, in general, the commanded torque τ_c is equal to $\overline{\tau}$, since this equality was assumed during the design process of the controller. Nevertheless, $f(\tau_c)$ is chosen slightly different in Equation 43 to limit the output to the maximum producible torque and to introduce a deadband by defining a minimum torque value τ_{min} that has to be reached or exceeded by the commanded torque to open thrusters.

DOI: 10.13009/EUCASS2023-464

$$f(\tau_c) = \begin{cases} \text{sign}(\tau_c)\,\tau_{max} & |\tau_c| > \tau_{max} \\ \tau_c & \tau_{min} \leq |\tau_c| \leq \tau_{max} \\ 0 & |\tau_c| < \tau_{min} \end{cases} \tag{43}$$

To determine γ_k and the corresponding time interval T_k, a design choice is made. It is desirable to keep the time intervals as short as possible to obtain the best fit prescribed by Equation 41, also for low frequencies. As a result, the restriction for T_k in Equation 40 should hold with equality whenever possible. The lowest value for $|f(\tau_c)|$, where the design choice still holds, is when both restrictions are fulfilled with equality. This value is defined as f_{min} in Equation 44.

$$f_{min} = \frac{\tau_{max}\, t_{on}}{t_{on} + t_{off}} \tag{44}$$

For values greater than f_{min}, the pulse γ_k is increased, such that the restriction in Equation 39 does not hold with equality anymore. If a value is less than f_{min}, the equality for the restriction in Equation 40 is relaxed and the time interval between successive pulses is larger than t_{off}. Using these relations, γ_k and T_k can finally be determined and are given in Equation 45 and Equation 46.

$$\gamma_k = \begin{cases} \frac{t_{off}\,|f(\tau_c)|}{\tau_{max} - |f(\tau_c)|} & |f(\tau_c)| \geq f_{min} \\ t_{on} & \text{otherwise} \end{cases} \tag{45}$$

$$T_k = \frac{\tau_{max}\,\gamma_k}{|f(\tau_c)|} \tag{46}$$

At each time step, γ_k and T_k are calculated and the time points when thrusters were last opened $t_{s,on}$ and closed $t_{s,off}$ are available. If thrusters are currently firing ($t_{s,on} > t_{s,off}$), the passed time since they were opened is compared to γ_k. If $t_{on} < \gamma_k$, the thrusters are commanded to continue firing, while they are closed otherwise. If thrusters are currently not firing, the time duration the thrusters are commanded to be closed can be calculated by $T_k - \gamma_k$ and a similar comparison is done. The entire algorithm and more details about this pulse modulation scheme can be found in Kienitz et al [4].

The described pulse modulation scheme assumes a perfect behavior of the thrust development, in fact an immediate reaction on open $\lambda_{on} = 0$ and close $\lambda_{off} = 0$ commands as well as an instantaneous realization of the target thrust value without any rise $\delta_r = 0$ or fall $\delta_f = 0$ time. In the ReFEx case, there are significant delays and transient behaviors, such that these assumptions do not apply. Therefore, the pulse modulation scheme is modified to compensate these characteristics. An exemplary command signal (abbreviated by "cmd"), its resulting normalized thrust (abbreviated by "real"), and the time constants are visualized in Figure 6.

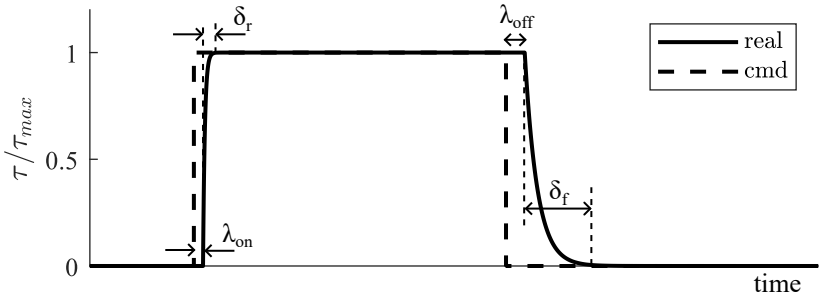

Figure 6: Comparison of a command signal and its real thrust reaction.

The time constants of the reaction control system depend on the thrust level and are slightly different every time a thruster is opened or closed. Their mean values are given in Table 2 and are further explained in Hoffmeister et al [3].

As mentioned before, the average torque value generated by the thrusters should be equal to the commanded torque. To achieve that, not only the function $f(\tau_c)$ has to be defined by Equation 43, but also the actual thrust curve has to match the expected one. As can be seen in Figure 6, the curves are quite different due to the time constants being greater than zero. Instead of comparing the average torque values, the impulse change generated over one time interval is investigated. Therefore, the areas below the curves have to be equal. Since λ_{off} and δ_f are greater than λ_{on} and δ_r,

DOI: 10.13009/EUCASS2023-464

Table 2: Mean time constants of the RCS.

	λ_{on} [ms]	δ_r [ms]	λ_{off} [ms]	δ_f [ms]
Low thrust	19.1	4.5	51.6	145.7
High thrust	25.6	5.3	53.0	139.0

the actual impulse change is larger than expected. To reduce it, a correction term $\Delta\gamma$ is implemented that closes the thrusters earlier. The term only depends on the behavior from a change in the command signal until the target value is reached, thus, it is independent of the duration of the pulse and as such a fixed value. The controller as well as the control allocation run on a frequency of 40 Hz, such that command changes can only be sent every 25 ms. As a result, the impulse changes match best for a correction term of 50 ms for both, low and high, thrust levels. The correction term is included in the algorithm by adapting the comparison in the Equation 47 and Equation 48.

$t_{s,on} > t_{s,off}$:

$$w(t_k) = \begin{cases} \text{sign}(f(\tau_c)) & t_k - t_{s,on} \leq \gamma_k - \Delta\gamma \\ 0 & \text{otherwise} \end{cases} \tag{47}$$

else:

$$w(t_k) = \begin{cases} 0 & t_k - t_{s,off} \leq T_k - (\gamma_k - \Delta\gamma) \\ \text{sign}(f(\tau_c)) & \text{otherwise} \end{cases} \tag{48}$$

Due to the properties of the reaction control system, the minimum pulse duration and the minimum rest between successive pulses are specified to $t_{on} = 25$ ms and $t_{off} = 175$ ms, respectively. Due to the modification of the pulse modulation scheme, these times are shifted by the correction term, such that t_{on} is set to 75 ms and t_{off} to 125 ms for the actual algorithm. Another value that still needs to be defined is the minimum torque value τ_{min} of Equation 43. To be consistent with the design choice, the shortest pulse duration at f_{min} should be applicable for the thrusters, while having reasonable acceleration to reduce errors and follow trajectories quickly. Considering the shifted t_{on} and t_{off} values, f_{min} results in 37.5 % of the maximum torque τ_{max}. Therefore, a slightly lower value of 35 % of the maximum torque value is chosen for τ_{min}.

Finally, the pulse modulator outputs $w(t)$ for the body axes need to be allocated to the eight cold gas thrusters as shown in Figure 2 while minimizing the risk of mission failure due to thruster malfunctions. Since the vehicle cannot detect faulty components during flight, the maximum number of thrusters is always utilized to generate the desired torque. Consequently, the roll torque τ_x and pitch torque τ_y commands partially utilize the same thrusters and can only be allocated together. If torques around the vehicle's x- and y-axes are commanded simultaneously, the pitch thruster that would counteract one of the roll thrusters is not utilized. A yaw torque τ_z can only be produced by thrusters 5 and 6. Therefore, there are no alternative options and these thrusters must not fail. A comprehensive overview of the thruster allocation for different combinations of torque commands is provided in Table 3. Since certain thrusters can be opened and closed by different pulse modulation outputs $w(t)$, it is not guaranteed that the restrictions outlined in Equation 39 and Equation 40 will apply to all thrusters. Furthermore, the scheme does not prevent a switch from $w(t) = 1$ to $w(t) = -1$, or vice versa, which would also result in a violation of the restrictions. Hence, before sending the on/off-commands to the actuator system, the minimum pulse duration and the minimum rest between successive pulses are additionally verified for each thruster.

Table 3: Allocation of the thrusters to the respective commanded torques (thruster setup in Figure 2).

	$+\tau_x$	$-\tau_x$	$+\tau_y$	$-\tau_y$	$+\tau_z$	$-\tau_z$
$+\tau_x$	2, 3	—	2, 3, 7	2, 3, 8	2, 3, 6	2, 3, 5
$-\tau_x$		1, 4	1, 4, 7	1, 4, 8	1, 4, 6	1, 4, 5
$+\tau_y$			1, 2, 7	—	1, 2, 7, 6	1, 2, 7, 5
$-\tau_y$				3, 4, 8	3, 4, 8, 6	3, 4, 8, 5
$+\tau_z$					6	—
$-\tau_z$						5

DOI: 10.13009/EUCASS2023-464

As already mentioned, the described control allocation design can compensate for single thruster failures in all directions except for the yaw direction and specific combinations of two faulty thrusters. A thruster is considered faulty if it does not open nor consume fuel. Generally, all valves for a roll motion and all combinations of a pitch thruster (number 7 and 8) and a roll thruster pointing in the same direction must not fail. The latter restriction arises from the fact that the remaining valve for the pitch direction and its opposite thruster cancel each other out, resulting in the inability to reduce pitch rate errors. The final list of compensable thruster failures is provided in Table 4. The numbers of the thrusters belonging to a particular combination are enclosed in square brackets.

Table 4: Compensable thruster failures.

Amount of failed Thrusters	Combinations
1	$[1] \vee [2] \vee [3] \vee [4] \vee [7] \vee [8]$
2	$[1,2] \vee [3,4] \vee [1,3] \vee [2,4] \vee [7,8] \vee [1,8] \vee [2,8] \vee [3,7] \vee [4,7]$

6. Performance Analysis

To finish the study, this section analyzes the performance of the exoatmospheric control system by simulation campaigns. The simulation environment utilized in the analysis is described in [6]. The evaluation focuses on various aspects, including the general functionality of the system, mode transitions, avoidance of overshoots, fuel consumption, and the impact of the correction term on the average generated torque. These investigations are conducted under nominal conditions, without any perturbations or uncertainties in the system. Subsequently, Monte-Carlo simulation results are employed to assess the robustness of the control system design. Finally, a scenario involving two thruster failures is compared to the nominal case to demonstrate the ability of the presented design to compensate for such failures.

6.1 Investigation of the Nominal Case

Figure 7 depicts selected signals, which are the total angle error θ_t and the measured angular rate $\boldsymbol{\omega}_m$, as well as the control inputs rate error ω_e and the quaternion error, expressed as angle errors θ_e for better interpretation. The total angle error is defined as the Euler angle of a single axis ($\boldsymbol{e}$) rotation that is needed to rotate from the current to the final reference attitude of a mode. It is therefore especially useful for the analysis of the sun acquisition mode (II) and entry attitude acquisition mode (V), since it indicates the required attitude change as well as the progress of the maneuver during the phase. Additionally, Figure 7a also shows the total angle errors around each body axis calculated by $(\theta_{t,x}\,, \theta_{t,y}\,, \theta_{t,z})^T = \boldsymbol{e}\,\theta_t$, while Figure 7b outlines the components of the measured angular rate $\boldsymbol{\omega}_m$ and its norm ω_m. The control inputs are visualized in a similar way. Furthermore, the measured angular rate is used to analyze the performance during the rate damping modes (I and IV), which aim to eliminate residual angular rates. At the same time, the measured angular rate is also useful to investigate the sun scanning mode (III), which commands a constant angular rate. The residual rate after separation is successfully reduced to values inside the gray box shown in Figure 7b, segment I, fulfilling the transition constraint of the RDM. The second RDM in segment IV has only a time constraint, but also reduces the measured angular rate effectively. The reorientations during SAM (II) and EAM (V) consistently reduce the total angle error and stay in the vicinity of the desired attitude. Thus, the attitude accuracy required at the end of SAM, visualized by the gray area in Figure 7a, can be achieved. At last, a constant roll rate during SSM (III) can be applied and maintained successfully.

The control errors in Figure 7c and Figure 7d do not show specific information about the modes, but visualize the performance of the controller in general. Both, the angle and the rate errors, are always bounded and large errors are successfully reduced. Moreover, it is not possible to determine a maximum attitude or rate error, since the limit angles of $\pm 0.42°$, mentioned in section 4, only define a threshold at which the thrusters start to open for a specific case and the proportional and derivative parts of the controller can counteract each other allowing larger state errors. In addition, the measured state can change rapidly due to changes of navigation errors. Furthermore, the rate error is also used as one of the transition constraints from SAM to SSM. The error at the end of the maneuver has to be inside the gray area shown in Figure 7d, which is actually fulfilled during the whole reorientation maneuver. As a result, Figure 7 shows the correct general functionality of the exoatmospheric control system and the mode switching logic.

DOI: 10.13009/EUCASS2023-464

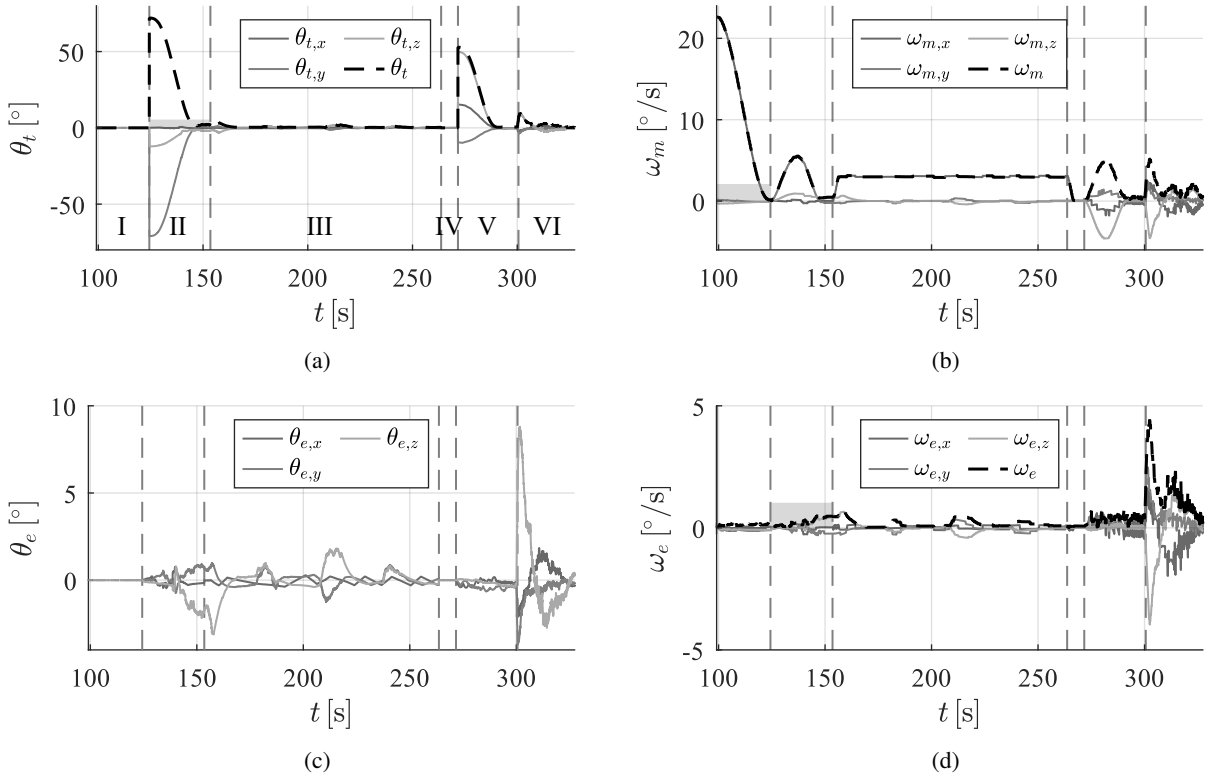

Figure 7: Exoatmospheric control errors and transition relevant signals for the nominal case. (a) Total angle error, (b) measured angular rate, (c) angle error and (d) angular rate error.

Next, the goal of aperiodic error dynamics due to the trajectory design and an overshoot prevention by setting the damping $\zeta = 1$ is analyzed by the pulse modulator outputs $\boldsymbol{\omega}$ for the sun acquisition mode in Figure 8. As can be seen by the commands, the maneuver is mainly performed around the body's y- and z-axes, thus, the thruster activity in roll direction only comprises few correction commands. The signals for pitch and yaw show only one sign change for the whole maneuver and almost no thruster activity at the end indicating an aperiodic motion of the vehicle. The last peak in Figure 8c is part of the limit cycle, since discrete firing actuators cannot achieve the desired state perfectly. Consequently, the aperiodic dynamics are sufficiently achieved resulting in a fuel efficient design.

The relative remaining fuel m_f for the reaction control system during the exoatmospheric flight is shown in Figure 9. While the sun scanning mode (III) consumes the least amount of fuel without considering the second rate damping mode (IV), most of the propellant is used during EAM and GEEM, since the actuators are operated in high thrust mode and aerodynamic disturbance torques begin to influence the vehicle. Most importantly, roughly 50 % of the fuel is left at the end of the exoatmospheric phase. Thus, a big margin remains to compensate for uncertainties and perturbations during the actual mission.

At last, the influence of the correction term on the generated average torque is investigated. Figure 10 shows the commanded torque around the vehicle's x-axis $\tau_{c,x}$ for the rate damping mode overlayed by the generated average torque of the thrusters $\overline{\tau}_x$. Here, the average value is obtained by applying a zero-phase low-pass filter on the actual torque signal. In contrast to Figure 10b, Figure 10a includes the correction term $\Delta\gamma$. Since the curves overlap better, $\Delta\gamma$ helps to generate the commanded torque more accurately. However, the overall performance is only marginally influenced.

6.2 Monte-Carlo Simulation Results

The robustness of the control system design is analyzed by means of 100 Monte-Carlo (MC) simulation results. Due to time intensive simulations, only small campaigns can be conducted currently, but an extensive Monte-Carlo campaign will be carried out later in the project. The exoatmospheric phase is influenced most by the perturbation of the initial

DOI: 10.13009/EUCASS2023-464

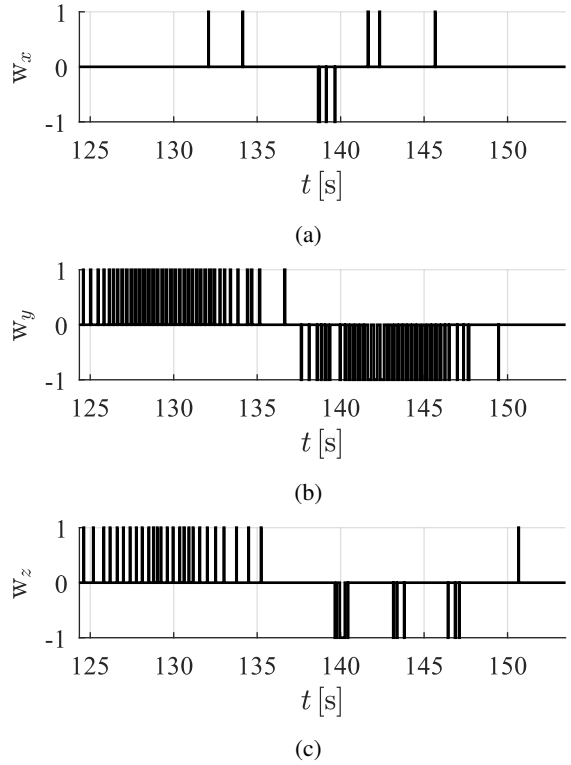

Figure 8: Pulse modulator outputs for SAM. (a) Roll, (b) pitch and (c) yaw.

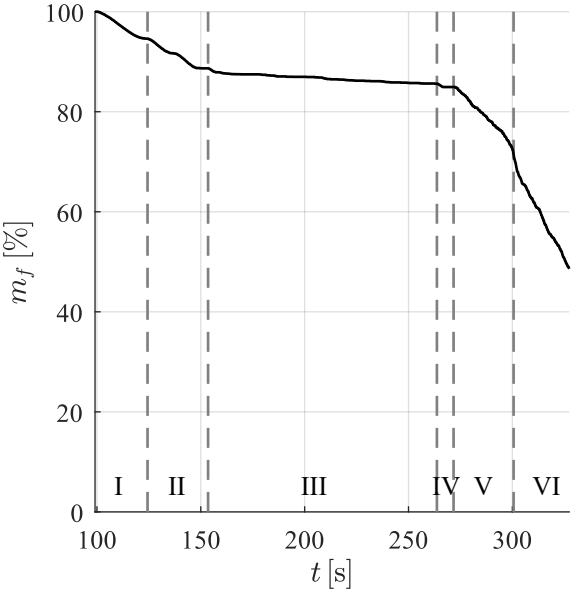

Figure 9: Remaining fuel for RCS.

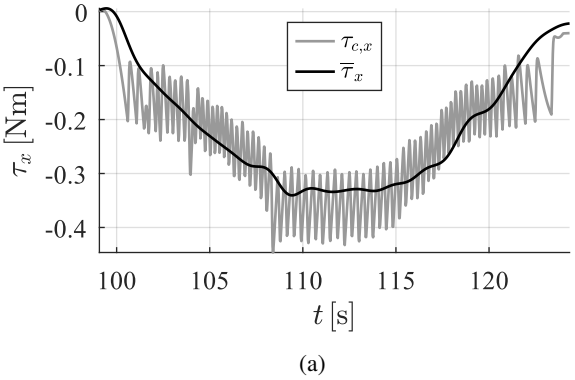

Figure 10: Influence of the correction term $\Delta\gamma$ on the generated average torque for RDM. (a) with $\Delta\gamma$ and (b) without $\Delta\gamma$.

state after separation, the mass properties of the vehicle, and the sensor and actuator properties. Figure 11 displays the total angle error θ_t and the norm of the measured angular rate ω_m during the several phases of the flight. The Monte-Carlo results that are shown in gray are overlayed by the nominal case in black (abbreviated by "nom"). To let all simulations start each phase at the same time, the results are cut in pieces. Since the flight durations are different for the simulations, the signals are not continuous as can be easily seen from the nominal case. Therefore, the time axis is not present in these figures. By comparing the Monte-Carlo results to the nominal case, the robustness can be investigated. For all modes and simulations, the errors are reduced sufficiently without a single simulation failing during the exoatmospheric flight. At the beginning of the sun scanning mode (III), the states differ significantly from the desired state due to the ongoing calibration process. But over the duration of the mode, θ_t and ω_m become more stable and accurate. In addition, it is noticeable that the perturbations of the maneuver during EAM are not distributed equally around the nominal case, but are mostly larger. Combined with the large errors at the beginning of SSM, most of the simulations consume more fuel than the nominal case, which can be seen in Figure 12. The relative remaining

DOI: 10.13009/EUCASS2023-464

fuel m_f is displayed over the duration of the exoatmospheric flight. Nevertheless, none of the simulations runs out of propellant and there is always at least roughly 20 % left. As a result, the control system design is sufficiently robust against expected perturbations and uncertainties with respect to the overall performance as well as the fuel consumption.

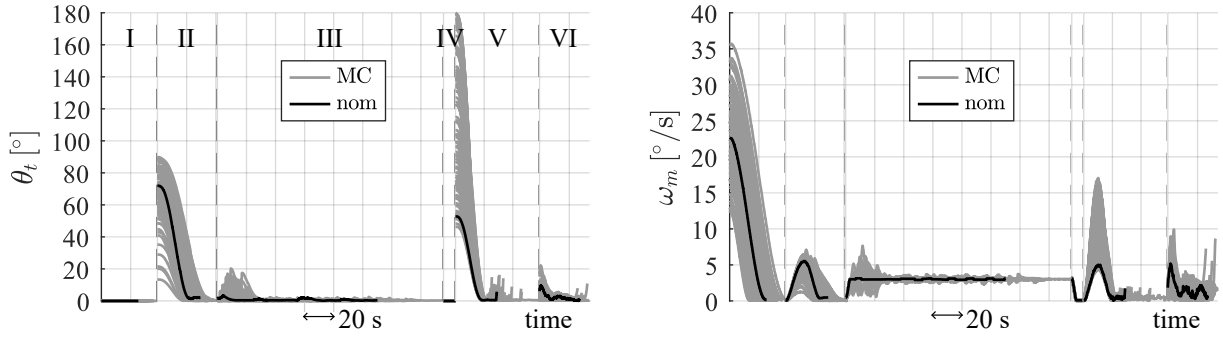

(a) (b)

Figure 11: Monte-Carlo results overlayed with the nominal case. (a) Total angle error and (b) norm of measured angular rate.

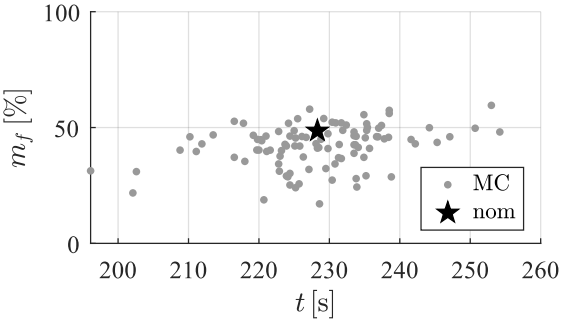

Figure 12: Remaining fuel for RCS at end of exoatmospheric flight for Monte-Carlo simulation and nominal case.

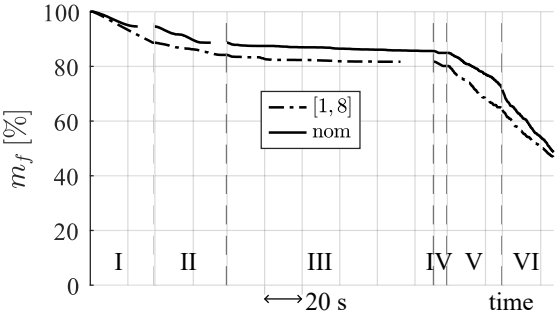

Figure 13: Comparison of remaining fuel for case with two failed thrusters and nominal case.

6.3 Compensation of Thruster Failures

In this subsection, a case with the failure of thrusters 1 and 8 (in figures denoted by $[1, 8]$) is investigated. Therefore, the total angle error θ_t and the measured rate ω_m are compared to the nominal case in Figure 14. Overall, every mode is executed indicating that all transition constraints could be achieved without a significant loss of accuracy. Hence, the vehicle is still fully controllable even with high precision. As a difference, the maneuvers of the rate damping mode (I) and the sun acquisition mode (II) take more time to complete. This results from a smaller angular acceleration as can be seen by lower gradients of ω_m in these phases. During EAM (V) the reorientations are limited by the predefined time $t_{1,dsgn}$ (see subsection 3.1), such that the maneuvers can actually be achieved in the same amount of time. Furthermore, the relative remaining fuel m_f, as shown in Figure 13, is quite similar at the end of the exoatmospheric flight with the failure case consuming slightly more. Since some roll and pitch torques cannot be generated decoupled, the failure case needs more fuel to reduce the residual rate after separation (I). In this specific simulation, it is compensated by GEEM (VI), where the nominal case consumes more propellant. However, this is considered to be a coincidence and a consequence of the deviated flight trajectory. In general, the coupled roll and pitch torques are always present, such that the overall fuel consumption should be a bit higher for the failure case compared to the nominal case. Nevertheless, the presented control allocation design can compensate certain combinations of undetected thruster failures without a noticeable loss of accuracy, but at the expense of a higher fuel consumption.

DOI: 10.13009/EUCASS2023-464

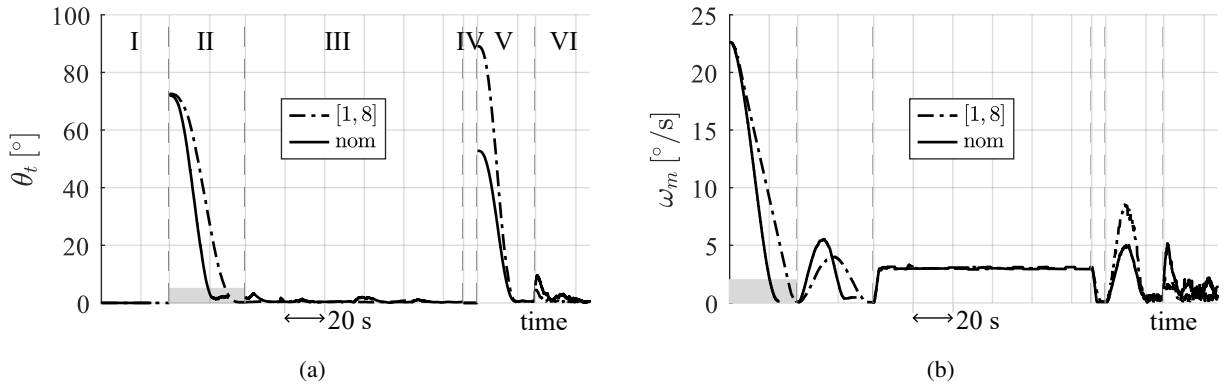

(a) (b)

Figure 14: Selected signals comparison for a case with two failed thrusters and the nominal case. (a) Total angle error and (b) norm of measured angular rate.

7. Conclusion

This paper presented the exoatmospheric control system for the DLR Reusability Flight Experiment (ReFEx), highlighting the benefits of combining trajectory planning and attitude error control. This approach allows for increased design flexibility, resulting in improved overall performance and fuel efficiency by avoiding overshoots and optimizing available time. Regarding trajectory planning, a quaternion interpolation algorithm based on spherical linear interpolation (SLERP) [2] has been applied to all corresponding modes during the exoatmospheric phase allowing to define attitude errors to be controlled by the flight control system. Regarding attitude control, partial feedback linearization of the Euler's moment equations [8] has been applied to reduce nonlinearities in closed-loop, enabling the use of pole placement to determine controller gains based on desired natural frequency and damping of the error dynamics while assuming approximate double-integrator closed-loop dynamics. A PD-controller commands the desired attitude control torques to a control allocation module which in turn transforms these commands into discrete firings of the reaction control system (RCS) using pulse-width pulse-frequency (PWPF) modulation. To provide attitude control considering switching restrictions and seamless transition between time intervals, a PWPF modulation scheme based on [4] and running on the same frequency as the controller was implemented, ensuring smooth operation and efficient control allocation by utilizing the maximum number of thrusters for each direction. This design allows for compensation of up to two undetected thruster failures with minimal loss of accuracy, except for the critical case of yaw thruster failure. Robustness analysis through Monte-Carlo simulations demonstrates the resilience of the control system, as all simulations successfully execute the exoatmospheric flight without running out of fuel (with a remaining fuel level above 20 %). Based on these results, the exoatmospheric control system is deemed well-prepared for the actual mission planned to be launched in 2024. Overall, the presented exoatmospheric control system is considered robust, efficient, and suitable for the upcoming mission.

8. Acknowledgments

The work described in this paper has been funded internally by the German Aerospace Center (DLR), Program Directorate Space Research and Technology, as part of the ongoing project Reusability Flight Experiment (ReFEx). The authors are very thankful for valuable discussions about the overall control system design with Johann Bals, Gertjan Looye, and Matthias Reiner. In addition, the authors would also like to thank Peter Kötting for his useful inputs regarding the trajectory planning and Jose Luis Redondo Gutierrez from the DLR Institute of Space Systems in Bremen for the invaluable collaboration and his infinite support regarding the simulation environment.

References

[1] Hyochoong Bang, Jung-Shin Lee, and Youn-Ju Eun. Nonlinear Attitude Control for a Rigid Spacecraft by Feedback Linearization. *KSME International Journal*, 2004.

[2] Erik B. Dam, Martin Koch, and Martin Lillholm. Quaternions, Interpolation and Animation. Technical report, Department of Computer Science, University of Copenhagen, 1998.

DOI: 10.13009/EUCASS2023-464

[3] Jonas Hoffmeister, Thorben Bruns, and Jens Gerstmann. ReFEx: Reusability Flight Experiment - Development of a cold-gas RCS using off-the-shelf components. *10th European Conference for Aerospace Sciences (EUCASS)*, 2023.

[4] Karl Heinz Kienitz and Johann Bals. Pulse modulation for attitude control with thrusters subject to switching restrictions. *Aerospace Science and Technology 9*, 2005.

[5] F. Landis Markley and John L. Crassidis. *Fundamentals of Spacecraft Attitude Determination and Control*. Springer, 2014.

[6] Jose Luis Redondo Gutierrez, Pablo Bernal Polo, Björn Gäßler, Johannes Robens, Paul Acquatella, David Seelbinder, and Stephan Theil. ReFEx: Reusability Flight Experiment - Architecture and Algorithmic Design of the GNC Subsystem. *10th European Conference for Aerospace Sciences (EUCASS)*, 2023.

[7] Peter Rickmers, Sebastian Kottmeier, and Guido Wübbels. ReFEx: Reusability Flight Experiment - A Demonstration Experiment for Technologies for Aerodynamically Controlled RLV Stages. *10th European Conference for Aerospace Sciences (EUCASS)*, 2023.

[8] Marcel J. Sidi. *Spacecraft Dynamics and Control, A Practical Engineering Approach*. Cambridge University Press, 1997.

[9] Jean-Jaques E. Slotine and Weiping Li. *Applied Nonlinear Control*. Prentice Hall, 1991.

[10] Bong Wie. *Space Vehicle Dynamics and Control*. American Institute of Aeronautics and Astronautics, second edition, 2008.